

Comparing numerical methods for hydrodynamics in a one-dimensional lattice spin model

Stuart Yi-Thomas,^{1,2,*} Brayden Ware,^{2,3} Jay D. Sau,^{1,2} and Christopher David White³

¹Condensed Matter Theory Center, University of Maryland, College Park, Maryland 20742-4111, USA

²Joint Quantum Institute, NIST/University of Maryland, College Park, Maryland 20742, USA

³Joint Center for Quantum Information and Computer Science,
NIST/University of Maryland, College Park, Maryland 20742, USA

(Dated: October 17, 2024)

In ergodic quantum spin chains, locally conserved quantities such as energy or particle number generically evolve according to hydrodynamic equations as they relax to equilibrium. We investigate the complexity of simulating hydrodynamics at infinite temperature with multiple methods: time evolving block decimation (TEBD), TEBD with density matrix truncation (DMT), the recursion method with a universal operator growth hypothesis (R-UOG), and operator-size truncated (OST) dynamics. Density matrix truncation and the OST dynamics give consistent dynamical correlations to $t = 60/J$ and diffusion coefficients agreeing within 1%. TEBD only converges for $t \lesssim 20$, but still produces diffusion coefficients accurate within 1%. The universal operator growth hypothesis fails to converge and only matches other methods on short times. We see no evidence of long-time tails in either DMT or OST calculations of the current-current correlator, although we cannot rule out that they appear at longer times. We do observe power-law corrections to the energy density correlator. At finite wavelength, we observe a crossover from purely diffusive, overdamped decay of the energy density, to underdamped oscillatory behavior similar to that of cold atom experiments. We dub this behavior “hot band second sound” and offer a microscopically-motivated toy model.

I. INTRODUCTION

Even at high temperature, where equilibrium states are simple, transport properties in strongly interacting materials can be hard to compute. The high-temperature regime is natural in cold-atom experiments such as the optical lattice transport experiments of 1 and 2. These experiments engineer the system’s Hamiltonian to have a low-energy subspace with dynamics governed by a Hamiltonian of interest, such as the Fermi-Hubbard model [1] or the Heisenberg model [2]. But thermalization and transport far from the ground state are also of interest in a wide variety of systems, from electronic materials such as cuprates and organic superconductors [3–9], which all display a rich finite-temperature phase diagram and non-Fermi-liquid behavior at high temperatures, to quark-gluon plasmas [10–14].

Numerically exact simulation of high-temperature dynamics is difficult for large systems or long times because it requires simulation of an exponentially large Hilbert space. But in systems that locally thermalize, one expects that sufficiently non-local operators have little effect on the dynamics of local operators, suggesting that simulations can track the local components of a Heisenberg-picture operator for long times without tracking non-local components. Indeed, Ref. 15 argues that in chaotic systems, one can simulate large systems to long times at a cost that is polynomial in size and time by truncating operators that are long compared to a thermalization length scale. A number of recently proposed

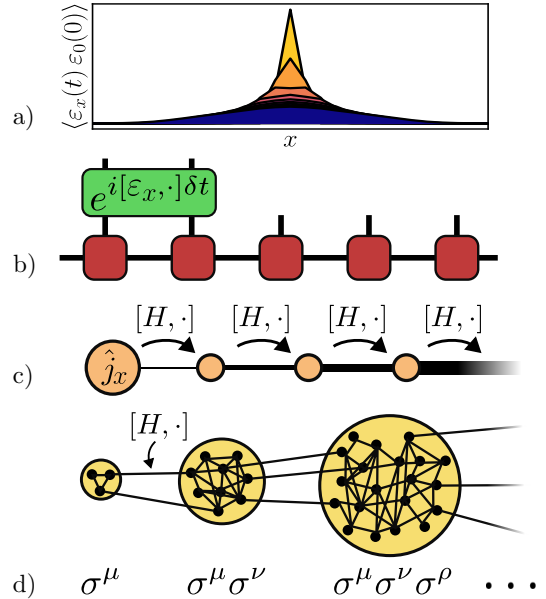


FIG. 1. Illustrations of **a)** the spreading of the energy-energy correlator over time, exhibiting diffusive hydrodynamics; **b)** TEBD on a tensor network MPS; **c)** Krylov dynamics mapped onto a half-chain with increasing couplings; **d)** connectivity of the Liouvillian graph, demonstrating lower coupling between operators with different diameters.

algorithms take advantage of this intuition, and approximately simulate high-temperature dynamics by truncating nonlocal components of Heisenberg-picture operators [16–20] — but they differ in the details of how the non-local components are truncated. It is unclear if these algorithms agree in their predictions and, if so, which

* snthomas@umd.edu

algorithm provides the most effective truncation scheme.

To resolve this question, we use four truncations of the operator dynamics—the recursion method with the universal operator growth hypothesis termination (which we abbreviate as R-UOG) [19], the operator-size truncated Liouvillian graph [20] (which we abbreviate as OST), time-evolving block decimation (TEBD) of matrix product operators with the usual SVD truncation [21–23], and TEBD with density matrix truncations (DMT) [16]—to compute infinite-temperature transport coefficients in the fruit-fly model for quantum dynamics, the non-integrable one-dimensional mixed-field Ising model. Infinite-temperature transport of the mixed-field Ising model was also studied in 17, 18, and 24 without comparing across methods. Because the methods differ in their underlying assumptions, our multimethod study offers an additional level of assurance in the common results beyond what can be provided by any one method, as well as a test of those underlying assumptions.

We find (Figs. 2 and 3) that DMT gives current-current correlators converged in bond dimension to time $t = 60$ and, consequently a diffusion coefficient that is converged to within 0.23% at bond dimension 256. OST agrees with these results to similar precision. This confirms the convergence testing of 20 and suggests that the operator chaos assumption of that work accurately models the system’s behavior. The R-UOG, by contrast, gives current-current dynamical correlation that agree with other methods only at short times $t \lesssim 4$, when the dynamics is controlled by the Lanczos coefficients exactly calculated. Beyond that time, the recursion method fails to converge in the number of exact coefficients (Fig. 6). This sensitivity suggests that the leading, universal behavior of the Lanczos coefficients misses some essential part of the dynamics.

We additionally investigate two questions about the physics of the nonintegrable mixed-field Ising model: the existence of hydrodynamic long-time tails and the origin of short-wavelength oscillatory modes [1, 25]. A hydrodynamic long-time tail is a power-law (as opposed to exponential) relaxation of the current-current correlator in time, originating from universal nonlinear corrections to the diffusion equation. We observe that in the non-integrable mixed-field Ising model, the current-current correlator displays exponential decay across three decades in magnitude. (We cannot rule out that the long-time tails appear at longer times.) We do, however, observe power-law corrections to the diffusive form of the energy density correlator. These corrections could result from nonlinear corrections to the diffusion equation, but they could also result from higher derivative terms.

Short-wavelength oscillatory modes were observed in cold atom experiments on the Fermi-Hubbard model [1]. Ref. 25 dubbed this phenomenon “hot band sound” and observed it in numerical simulations of a kinetically constrained model with particle number conservation. We give numerical evidence that the fruit-fly non-integrable Hamiltonian, which does not conserve particle number,

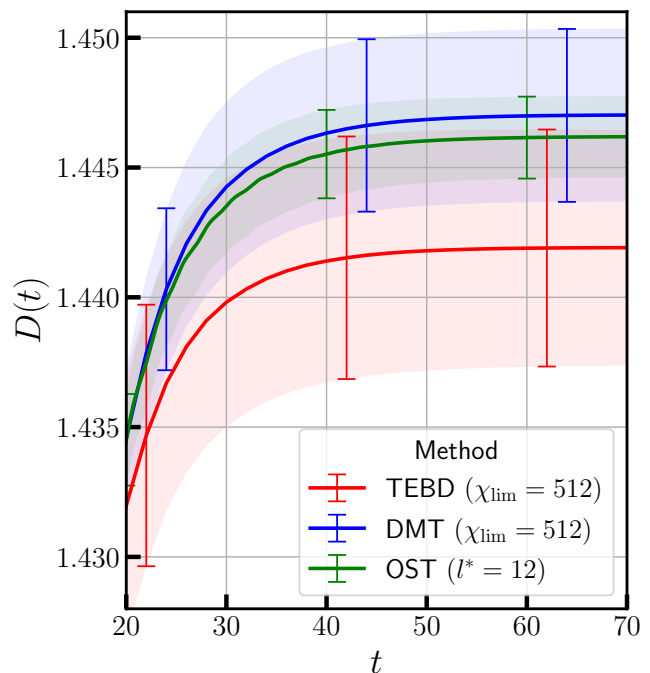


FIG. 2. Time-dependent diffusion coefficient $D(t)$ (Eq. 12) for TEBD, DMT, and OST dynamics. Error bars show bond dimension convergence error: for TEBD and DMT, the absolute value of the difference between the largest bond dimensions ($|D_{\chi_{\text{lim}}=512}(t) - D_{\chi_{\text{lim}}=256}(t)|$); and for OST dynamics the absolute value of the difference between preservation diameters ($|D_{l^*=12}(t) - D_{l^*=11}(t)|$) at loss rate $\gamma_{\text{semi-emp.}}$ (Eq. 24). TEBD and DMT are subject to Trotter error, which turns out to be negligible (see Appendix B). For comparison, DAOE [15, Fig. 3.] gives a long-time diffusion coefficient $\approx 1.4 \pm 0.01$.

also has short-wavelength oscillatory modes in the energy density. We dub these modes “hot band second sound” and we give a physical picture for how these oscillatory modes emerge.

The paper is organized as follows. In Sec. II, we discuss our model (the Ising model model with transverse and longitudinal fields) and the phenomenology we expect: diffusion at leading order in frequency and wavelength, with higher-order corrections. In Sec. III we describe the methods we use. In Sec. IV we give the results of the four methods for the current-current correlator. And in Sec. V we describe the model’s short-wavelength “hot band second sound” phenomenon.

II. MODEL AND PHENOMENOLOGY

A. Model

We consider spin chains described by nonintegrable, translationally invariant, parity-symmetric, and time-independent Hamiltonians with no additional symmetries. Such systems have just one local conserved quan-

tity, the energy density. We use the spin-1/2 Ising model with both transverse and longitudinal fields

$$H = \sum_i 4JS_i^z S_{i+1}^z + 2g_z S_i^z + 2g_x S_i^x. \quad (1)$$

where $S^a = \frac{1}{2}\sigma^a$ are spin operators. This model is well-studied in the context of hydrodynamics [16, 17, 20, 26] and follows the ETH in a strong sense [27]. In this paper, we set $J = 1$, $g_x = 1.4$, and $g_z = 0.9045$ for consistency with other work on numerical methods for hydrodynamics [16, 17]. These particular values of the parameters are chosen to ensure that the model is far from the integrable lines $g_z = 0$ or $g_x = 0$, and similarly far from the near-integrable physics that occurs when g_x or g_z is large. Our results should not change qualitatively as long as J , g_x , and g_z are all of similar magnitude.

In matrix product operator (MPO) simulations, we work with large but finite systems ($L = 256$), stopping the simulations before the bond dimension near the boundary becomes greater than 1. R-UOG and the OST dynamics can be formulated directly in Fourier space, so in those simulations we work with formally infinite systems.

B. Phenomenology

Ergodic quantum systems, such as the non-integrable spin chains under study in this paper, approach thermal equilibrium under their own dynamics. When the dynamics conserves some charge, the approach to equilibrium is generically described at the largest scales by *hydrodynamics*. Hydrodynamics is a classical effective description derived by assuming that the state is locally similar to the maximum entropy state with constrained values of the density of conserved charges. This assumption only makes sense as a coarse-grained, approximate description [28, 29]; the hydrodynamic equations are irreversible, unlike the true microscopic dynamics. (One goal of 15 and 20 is to provide a microscopic justification for this irreversibility.)

Consider a spin chain with a single local conserved quantity. In this paper, the conserved quantity will be an energy density operator

$$\hat{\varepsilon}_x = 4JS_x^z S_{x+1}^z + g_z(S_x^z + S_{x+1}^z) + g_x(S_x^x + S_{x+1}^x). \quad (2)$$

The corresponding local current operator \hat{j}_x is defined via the local conservation law

$$\partial_t \hat{\varepsilon}_x = -\Delta \hat{j} = \hat{j}_{x-1} - \hat{j}_x. \quad (3)$$

which for energy density in Eq. 2 yields¹

$$\hat{j}_x = 4g_x (S_x^y S_{x+1}^z - S_{x-1}^z S_x^y) \quad (4)$$

The assumption underlying hydrodynamics is that the system's state, including currents, is entirely determined by the values of the local conserved charge density; thus $j(x) = \langle \hat{j}_x \rangle$ is a functional of the profile of $\varepsilon(x) = \langle \hat{\varepsilon}_x \rangle$ [28, 29]. Because the dynamics are local, we can expand j in gradients of ε :²

$$\begin{aligned} j = & -D\partial_x \varepsilon + F_1 \partial_x^3 \varepsilon + F_2 \partial_x^5 \varepsilon \dots \\ & + F_3 \varepsilon \partial_x \varepsilon + F_4 \varepsilon \partial_x^3 \varepsilon + \dots \\ & + F_5 \varepsilon^2 \partial_x \varepsilon + F_6 \varepsilon^2 \partial_x^3 \varepsilon + \dots \\ & + F_7 (\partial_x \varepsilon)^3 + \dots \end{aligned} \quad (5)$$

At leading order in momentum and in the variation in ε , the gradient expansion becomes $j = -D\partial_x \varepsilon$, so the energy ε follows the diffusion equation

$$\partial_t \varepsilon = -D\partial_x^2 \varepsilon. \quad (6)$$

Transport of the energy density ε can be studied with the two-point correlation function

$$C^{\varepsilon\varepsilon}(x, t) = \langle \hat{\varepsilon}_x(t) \hat{\varepsilon}_0(0) \rangle \equiv \text{Tr} [\hat{\varepsilon}_x(t) \hat{\varepsilon}_0(0) \rho_{\text{eq}}], \quad (7)$$

where the expectation value is taken with respect to an equilibrium state ρ_{eq} . In linear response, this correlation function measures the spread of an infinitesimally small bump in energy density initially located at $x = 0$. We can define a variance

$$V(t) = \frac{\sum_x x^2 C^{\varepsilon\varepsilon}(x, t)}{\sum_x C^{\varepsilon\varepsilon}(x, t)}. \quad (8)$$

The denominator

$$\nu \equiv \sum_x C^{\varepsilon\varepsilon}(x, t) = \frac{1}{L} \text{Tr} H^\dagger H \quad (9)$$

is time-independent by the conservation of energy. For the Hamiltonian in (1), $\nu = J^2 + g_z^2 + g_x^2$.

In a system where the energy ε undergoes diffusion, $C^{\varepsilon\varepsilon}(x, t)$ asymptotically takes the form of a Gaussian with a spatial variance $V(t)$ that increases linearly in time:

$$C^{\varepsilon\varepsilon}(x, t) \sim \frac{1}{\sqrt{2\pi V(t)}} \exp \left[-\frac{x^2}{2V(t)} \right], \quad (10a)$$

$$V(t) \approx 2Dt. \quad (10b)$$

¹ There is a gauge ambiguity in the definition of $\hat{\varepsilon}_x$ and \hat{j}_x , as rewriting $\hat{\varepsilon}_x \rightarrow \hat{\varepsilon}_x + \hat{a}_{x+1} - \hat{a}_x$ for any local operator \hat{a}_x yields the same total energy \hat{H} up to a boundary term. Following Ref. 30, we assume that $\hat{\varepsilon}_x$ is chosen in a translationally invariant and PT-symmetric manner.

² Even-order derivatives disappear because the current is odd under inversion symmetry.

Even for diffusive systems, Eq. 10b only holds in the long-time limit. To understand how the system approaches that long-time limit (and to treat systems that may be super- or sub-diffusive), we define a time-dependent diffusion coefficient

$$D(t) = \frac{1}{2} \frac{d}{dt} V(t) \quad (11)$$

using the variance in Eq. 8. In the special case of a diffusive systems, $D(t)$ approaches a constant D in the long-time limit. In general—that is, without assuming diffusion—the conservation law (3) relates the time-dependent diffusion coefficient $D(t)$ to the autocorrelation of the total current operator $\hat{J} = \sum_x \hat{j}_x$ [31], assuming time- and spatial-translation invariance:

$$D(t) = \frac{1}{\nu} \int_0^t dt' \sum_x \langle \hat{j}_x(t) \hat{j}_0(0) \rangle \quad (12a)$$

$$= \frac{1}{L\nu} \int_0^t dt' \langle \hat{J}(t') \hat{J}(0) \rangle. \quad (12b)$$

Much of this paper treats the current autocorrelation function to calculate $D(t)$. Derivations of these correlators, as well as a comparison of the resultant values of $D(t)$, are found in Appendix A. Neither the value of D nor the other coefficients in Eq. 5 are straightforwardly derived from the microscopic equations of motion.

For finite times, $D(t)$ may be sensitive to the nonlinear-in- ε corrections F_3, F_4, F_5, \dots of the gradient expansion of the current (5). In particular, these nonlinear corrections can lead to *long-time tails* [32]: roughly, algebraic decay of $D(t)$ to its long-time value. When computing the diffusion coefficient via the correlator $\langle J(t)J(0) \rangle$, as in Eq. 12, many of the terms in the gradient expansion given by Eq. 5 disappear. In particular, terms of the form $\varepsilon^n \partial_x \varepsilon^l$ become total derivatives. Since $\lim_{x \rightarrow \pm\infty} \langle \varepsilon(x) \rangle = 0$, these must integrate to zero. For systems with a single conserved charge, the lowest-order term that is not of this form is $(\partial_x \varepsilon)^3$; in Eq. 12 the term $(\partial_x \varepsilon)^3$ does not become an integral of a total derivative, though we cannot rule out the possibility that it disappears for other reasons.³ (One of our results is that if $(\partial_x \varepsilon)^3$ contributes to the integral in (10), its effect is small.)

These long-time tails do not exhaust the system's potential finite-wavelength and finite-frequency dynamics. To probe short-wavelength physics beyond leading-order hydrodynamics, we also analyze the Fourier transform of the charge-charge correlator

$$C^{\varepsilon\varepsilon}(k, t) = \langle \varepsilon(k, t) \varepsilon(k, 0) \rangle = \sum_x e^{-ikx} C_x^{\varepsilon\varepsilon}(t). \quad (13)$$

For a strictly diffusive system $C^{\varepsilon\varepsilon}(k, t) \propto e^{-Dk^2 t}$, but non-diffusive short-wavelength and high-frequency dynamics can lead to other forms. This correlator measures the system's response to a drive, so many experiments can probe it or its time Fourier transform [33]. It is also used to analyze the quantum gas microscope experiment of 1 and 34.

III. METHODS

To compute the correlators discussed in the previous sections, we use several methods for evolving operators. Two of the methods—TEBD and TEBD with density matrix truncation (DMT)—approximate the evolving operator as a matrix product operator (MPO) in a real space basis, as illustrated in Fig. 1(b). DMT differs from TEBD in that it guarantees that local expectation values are preserved during truncation. These methods are further discussed in Sec. III A 1 and Sec. III A 2 respectively.

The other two methods, the recursion method with universal operator growth hypothesis (R-UOG, Sec. III B) and the operator size truncated dynamics (OST, Sec. III C), both represent Heisenberg dynamics as single-particle hopping on a graph. The recursion method maps the Heisenberg dynamics of the operator to single-particle hopping on a half-infinite chain with hopping coefficients—called Lanczos coefficients—computed via repeated commutators with the Hamiltonian, as illustrated in Fig. 1(c). The truncated Liouvillian graph likewise maps the Heisenberg dynamics of the zero-momentum current operator to single-particle hoppings on a graph, but now the graph has vertices labeled by Pauli strings and edges specified by the Hamiltonian, as illustrated in Fig. 1(d). The dynamics among Pauli strings with small diameter is treated exactly, with the coupling to larger operators replaced by an effective dissipative boundary, as proposed by one of the authors in Ref. 20.

A. Matrix product operator methods

To compute the current Green's function (12a) using TEBD simpliciter (Sec. III A 1) or TEBD with density matrix truncation (DMT, Sec. III A 2), we construct an matrix product operator (MPO) representation of $\hat{j}(t) = e^{-iHt} \hat{j}(0) e^{iHt}$. Equation 12a then gives the Green's function for time t . For long times, we use time-doubling (Appendix C) to calculate results up to $2t$ using the same MPO. In Sec. V we compute the energy density Green's function (13) analogously using DMT.

1. TEBD

Time-evolving block decomposition [21, 22] applies a Trotterized time evolution to a matrix product state or

³ 32 analyzed systems with multiple conserved quantities q_α . In that context, the first nonlinear correction that is not an integral of a total derivative is a second order term $j_\alpha \propto \dots + E_{\alpha\beta\gamma} q_\beta \partial_x q_\gamma$.

matrix product operator [23]. (For an exhaustive review of matrix product state methods, see 35). We use a fourth-order Trotterization [36, Eq. 32 ($m = 13$, type SL, $\nu = 3$)].

Each gate application increases the MPO bond dimension, but the resulting state may have a good approximation with lower bond dimension. TEBD chooses the approximate MPO that minimizes the L_2 distance $\text{Tr}(\rho - \rho_{\text{approx}})^2$. TEBD truncation generically changes the system's conserved quantities and currents.

2. DMT

Density matrix truncation (DMT) [16] uses the same limited bond dimension MPO approximation as TEBD, while guaranteeing that local expectation values—including conserved quantities and currents—are unchanged in the truncation process. It does this by performing a gauge transformation on the virtual space that separates correlations on length scales less than some controllable length from longer-range correlations, and discarding small principal components of the long-range correlations. We describe the method in some detail in App. D. DMT as presented in 16 was designed for Schrödinger dynamics of density matrices and uses the fact that those density matrices have nonzero trace. We use a variant of DMT slightly modified for Heisenberg evolution of traceless operators (Appendix D).

B. Recursion method with universal operator growth hypothesis termination (R-UOG)

The recursion method is a general tool for dynamics that derives from the Lanczos tridiagonalization algorithm [37, 38]. We follow the implementation of the method in Ref. 19.

As in all Lanczos-derived algorithms, the computation begins by the construction of an orthonormal basis for the space of vectors generated by the repeated action of an operator. We consider the Hamiltonian dynamics of operators generated by the Liouvillian superoperator $\mathcal{L} = [H, \cdot]$ and initial operator $\mathcal{O}_0 = J$, the energy current. We use the trace inner product to define orthonormality. The recursion method then constructs an orthonormal basis for the space of operators spanned by repeated commutations of the Hamiltonian with the current operator:

$$\begin{aligned} \{\mathcal{O}_0 = J, \mathcal{O}_1 = \mathcal{L}(\mathcal{O}_0), \mathcal{O}_2 = \mathcal{L}(\mathcal{O}_1) \dots\} \\ = \{J, [H, J], [H, [H, J]], \dots\}. \end{aligned} \quad (14)$$

The orthonormal basis $\{B_k\}$ is generated by the Gram-Schmidt procedure, which can be expressed through the

recurrence relation

$$\begin{aligned} b_k &= \left(\text{Tr} A_k^\dagger A_k \right)^{1/2} \\ B_k &= b_k^{-1} A_k \\ A_{k+1} &= \mathcal{L} B_k - b_k B_{k-1}. \end{aligned} \quad (15)$$

The recursion is initialized with $A_0 = \mathcal{O}_0 = J, B_{-1} = 0$. In the basis $\{B_k\}$, the Liouvillian takes a tridiagonal form with coefficients given by b_k :

$$\mathcal{L}_{\text{eff}} = \begin{bmatrix} 0 & b_1 & & & \\ b_1 & 0 & b_2 & & \\ & b_2 & 0 & \ddots & \\ & & & \ddots & \ddots \\ & & & & & \ddots \end{bmatrix}. \quad (16)$$

Once b_k and B_k are computed, the time evolution

$$J(t) = e^{-i\mathcal{L}t} J \quad (17)$$

can be computed using the effective tridiagonal Liouvillian \mathcal{L}_{eff} . This maps the evolution problem to that of a particle hopping on a half-infinite, one dimensional chain, as depicted in Fig. 1(c), with hopping coefficients b_k .

We work directly in the thermodynamic limit, where the recursion never ends. The recursion coefficients can be computed with finite memory using a sparse, momentum space representation of the operators that stores only non-zero coefficients in a Pauli operator basis. The computational cost for each successive step grows exponentially in the Lanczos order k due to the combinatorial explosion of the number of terms in the repeated commutators. In practice, a maximum of $k^* \sim 20\text{--}30$ Lanczos coefficients can be exactly computed.

The recursion method handles this limitation by choosing a termination of the half-infinite chain appropriate to the dynamics at hand [38]. A hard-wall termination at k^* is a particularly bad choice: due to reflections off the end of the chain, such a time-evolution predicts unphysical revivals of the current. Ref. 19 proposes instead to continue the chain indefinitely, using an ansatz—the *universal operator growth hypothesis*—to approximate the Lanczos coefficients b_k for $k > k^*$. They give persuasive evidence that generic, ergodic, one-dimensional spin chains have coefficients b_k that scale asymptotically as $b_k \sim k / \log k$.

We therefore fit the computed ($k \leq k^*$) Lanczos coefficients to a form

$$b_k = ak / \log k + c, \quad (18)$$

and compute the dynamics using Lanczos coefficients

$$b'_k = \begin{cases} b_k & k \leq k^* \\ ak / \log k + c & k^* < k \leq K \end{cases} \quad (19)$$

with the fit parameters a, c extracted from the first k^* coefficients. For our purposes, K is taken to be any value

that is large enough to ensure the operator does not reach the boundary within the time of the simulation. As an alternative, one can use a Green's function termination at site K to appropriately account for the dynamics on the remainder of the chain [19, 38].

C. Operator-size truncated Liouvillian graph with a priori decay (OST)

Instead of mapping Heisenberg dynamics to single-particle hopping on a one-dimensional half-infinite chain, the picture of 20 maps it to a more complicated graph, whose vertices are Pauli strings and whose edges are given by matrix elements of the Liouvillian. This graph is called the Liouvillian graph; it was introduced in 39. In the OST dynamics of 20, the structure of this graph, together with a chaos assumption on the dynamics of operators that act nontrivially on many sites, leads to a strongly-interacting analog of Boltzmann's Stosszahlansatz [40, 41]—his assumption that correlations between particle velocities can be ignored. This in turn leads to a tractable non-Hermitian effective model of the dynamics of short operators.

The Heisenberg dynamics of an operator $A = \sum_{\mu} A_{\mu} \sigma^{\mu}$, where σ^{μ} are Pauli strings, is

$$\frac{d}{dt} \sum_{\mu} A_{\mu} \sigma^{\mu} = \sum_{\mu} i[H, \sigma^{\mu}] A_{\mu}. \quad (20)$$

This is exactly equivalent to a single particle hopping between sites labeled by the Pauli strings σ^{μ} with amplitudes given by the commutator:

$$\begin{aligned} H_{\text{graph}} &= \sum_{\mu\nu} L_{\mu\nu} c_{\mu}^{\dagger} c_{\nu} \\ L_{\mu\nu} &= 2^{-L} \text{Tr} [\sigma^{\mu} [H, \sigma^{\nu}]]. \end{aligned} \quad (21)$$

For a local Hamiltonian almost all of the $L_{\mu\nu}$ are 0, so it is useful to think of the Hamiltonian (21) as hopping on a graph whose vertices are the Pauli strings and whose edges are pairs (μ, ν) with $L_{\mu\nu} \neq 0$. [39].

The Liouvillian graph has a natural subgraph structure. Any one Pauli string is connected to many other Pauli strings of the same length, but very few larger or smaller strings. More explicitly, define the *diameter* of a Pauli string $\text{diam } \sigma^{\mu}$ to be the distance between the first site on which it acts nontrivially and the last—that is, the diameter of the Pauli string's support. Write

$$\mathcal{G}_l = \{ \sigma^{\mu} : \text{diam } \sigma^{\mu} = l \};$$

where \mathcal{G}_l is the *pool of diameter l* . If the Hamiltonian generating the Liouvillian graph is local, there are $O(l)$ Hamiltonian terms that can commute with some $\sigma^{\mu} \in \mathcal{G}_l$ to produce other Pauli strings in \mathcal{G}_l , but only $O(1)$ terms that can produce Pauli strings in $\mathcal{G}_{l\pm 1}$. The pools \mathcal{G}_l are therefore tightly intracommuted, but loosely interconnected.

Moreover, if the physical Hamiltonian is not integrable, the dynamics of the graph Hamiltonian restricted to a pool \mathcal{G}_l is chaotic. Its eigenoperators have support on all the Pauli strings in \mathcal{G}_l , its eigenenergies display GOE or GUE level-spacing statistics, and its density of states is (approximately) Gaussian. For large l , then, the dynamics of the pool l are completely characterized by the Gaussian Green's function

$$\begin{aligned} G_{\lambda\lambda;l}(t) &\equiv \langle \lambda | \exp[-iH|_{\mathcal{G}_l} t] | \lambda \rangle \\ &\approx e^{-\gamma_l^2 t^2} \end{aligned} \quad (22)$$

where $H|_{\mathcal{G}_l}$ is the restriction of the graph Hamiltonian (21) to the pool \mathcal{G}_l , λ is some operator in \mathcal{G}_l , and γ_l is the width of the density of states

$$\gamma_l^2 = \frac{1}{|\mathcal{G}_l|} \text{Tr} H|_{\mathcal{G}_l}^2. \quad (23)$$

The Green's function (22) is broadly independent of the operator λ if $H|_{\mathcal{G}_l}$ is chaotic, as it is for the mixed-field Ising model. For the mixed-field Ising model (1) this is $\gamma_l^2 = l(J^2 + g_x^2 + g_z^2)$. Ref. 20 found that the dynamics on all pools with diameter l or larger, i.e. $\bigcup_{l' \geq l} \mathcal{G}_{l'}$, is better characterized by a semi-empirical decay rate

$$\gamma_{\text{semi-emp.}} = \sqrt{(l+1)(J^2 + g_x^2 + g_z^2)}. \quad (24)$$

The physical picture behind (22) is that our single particle can hop onto a site in the pool \mathcal{G}_l and stay there for a time $\sim \gamma_l^{-1}$, during which it can hop back to the pool, say \mathcal{G}_{l-1} , from which it came.⁴

This physical picture suggests that we pick some l , call it l_* , and replace the dynamics on operators longer than l_* by a memory kernel [42, 43] (see 33, chapter 5 for a helpful introduction) given by the Green's function (22). This would lead to an unpleasant integro-differential equation. Instead, we (following 20) replace the Gaussian Green's function (22) by an exponential memory kernel. The result is a non-Hermitian effective Hamiltonian

$$\begin{aligned} H_{\text{graph;eff}}(\gamma, l_*) &= \sum_{\mu, \nu \in \mathcal{G}_{\leq l_*}} L_{\mu\nu} c_{\mu}^{\dagger} c_{\nu} + \text{h.c.} \\ &\quad - i\gamma \sum_{\nu \in \mathcal{G}_{l_*+1}} c_{\nu}^{\dagger} c_{\nu}. \end{aligned} \quad (25)$$

In principle γ is set by the semi-empirical prediction (24), but we will find it enlightening to consider how the behavior of the effective model depends on the decay rate γ , so we leave it as a parameter.

⁴ We assume the particle is very unlikely to hop back down to \mathcal{G}_{l-1} after it has left the first site in \mathcal{G}_{l-1} it hopped to. 20 offers numerical evidence that this is the case and intuition for how it comes about; 15 offers more careful combinatorial arguments about a related question.

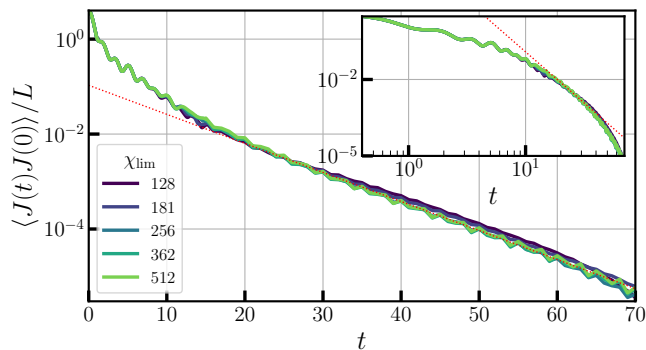


FIG. 3. Current-current correlator computed with DMT, across bond dimension caps χ_{lim} . The correlator displays approximately three decades of exponential decay (for $20 \lesssim t \lesssim 70$) at decay rate 0.14 (red dotted line). The inset demonstrates the lack of a predicted [32, 45] $\sim t^{-4}$ (red dotted line) power law via a logarithmic time axis. This plot shows Trotter step $\tau = 0.05$ for $t < 15$ and $\tau = 0.5$ with time-doubling (see Appendix C) for $t > 15$; Fig. 11 shows convergence in Trotter step.

As long as the underlying physical Hamiltonian is translation invariant, the effective graph Hamiltonian can be directly constructed in Fourier space. We do so throughout this paper. We use Krylov subspace methods to simulate the dynamics generated by the effective Hamiltonian (25) [44].

The OST dynamics is motivated in part by DAOE [17], but differs substantially in how it treats the operator Hilbert space. DAOE keeps the whole operator Hilbert space, but modifies the evolution by adding an artificial dissipation on large-weight operators. Because DAOE uses matrix product operators as the underlying data structure, it can represent operators in a manifold (the low-bond-dimension manifold) that includes a complete basis for that Hilbert space; the artificial dissipation keeps the system in or near that low-bond dimension manifold. OST dynamics, by contrast, truncates the Hilbert space—it discards operators of diameter greater than l_* —and models the effect of those operators on the small-diameter operators by a decay.

The OST dynamics differs from the dynamics of 39 in how it truncates the Liouvillian graph. The dynamics of 39 imposes an absorbing boundary condition at a fixed graph distance from an initial seed operator. The OST dynamics [20] instead puts the absorbing boundary at a natural subgraph partition of the Liouvillian graph, and motivates the absorbing boundary condition using the chaos properties of the subgraph dynamics.

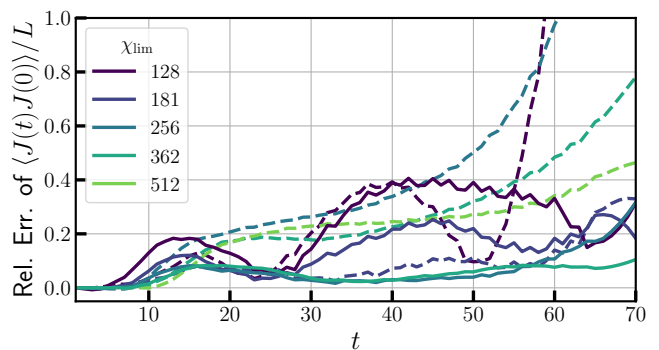


FIG. 4. The relative error of TEBD (dashed lines) and DMT (solid lines) current correlators against the $\chi_{\text{lim}} = 512$ DMT series, smoothed with a second order Savitzky-Golay filter (computed using `scipy` [46]) with window width of $m = 12$. We smooth because low bond dimension DMT does not accurately capture the oscillatory behavior of the converged large-bond dimension simulations. This oscillatory behavior has a limited effect on the diffusion coefficient. We show the unsmoothed relative error in Appendix E, Fig. 12.

IV. CURRENT-CURRENT CORRELATOR

A. Exponential decay of current-current correlator

Fig. 3 shows the current-current correlator as a function of time as computed in DMT with time-doubling. The correlator displays a fast decay for $t \lesssim 20$, and an exponential decay for $20 \lesssim t \lesssim 60$ with decay rate ≈ 0.14 . In this context, we define convergence as the relative error between $\chi_{\text{lim}} = 256$ and $\chi_{\text{lim}} = 512$ less than 0.15, as shown in Fig. 4 (also see Fig. 12). Because $D(t)$ is dominated by early-time contributions, convergence in $D(t)$ (Fig. 2) is much better than late-time convergence in $\langle J(t)J(0) \rangle$ (Fig. 3). The $t > 15$ data are computed with a relatively large time step of size $\tau = 0.5$ and combined with data computed using a finer time step of size $\tau = 0.05$ to increase the accuracy of the numerical integral for $D(t)$. We show convergence in Trotter step in Appendix E.

At long times, the correlator displays a curious oscillation about an overall exponential decay. This decay and oscillation can be phenomenologically characterized using three poles as

$$\langle J(t)J(0) \rangle \sim Ae^{-z_0 t} + Be^{-z_1 t} + B^* e^{-z_1^* t}, \quad t \gtrsim 20 \quad (26)$$

with $z_0 \approx 0.14$ a purely real decay rate and $z_1 \in \mathbb{C}$ a decay $\text{Re } z_1$ combined with an oscillation $\text{Im } z_1$. The amplitude of the oscillation changes little over the time $20 \lesssim t \lesssim 70$ so the real part of z_1 is fine-tuned to be close to z_0 :

$$|z_0 - \text{Re } z_1| \lesssim 1/70. \quad (27)$$

Based on Fig. 3 we cannot rule out that $z_0 > \text{Re } z_1$, which would lead to $\langle J(t)J(0) \rangle < 0$ at sufficiently long times.

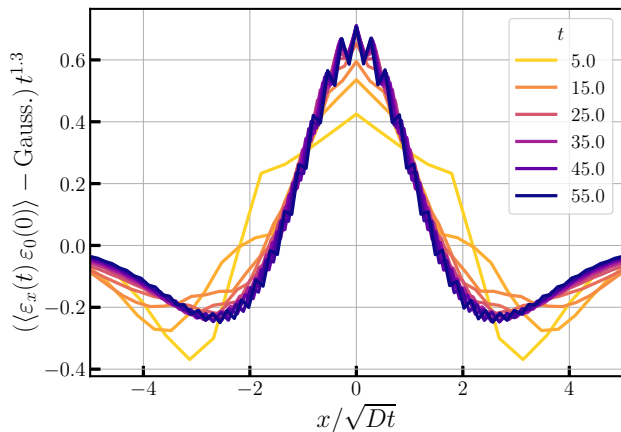


FIG. 5. Power-law corrections to diffusion in the energy-energy correlator, rescaled by $t^{1.3}$. The corrections are generated by subtracting a Gaussian with a variance of $2Dt$ with a diffusion constant of $D = 1.446$ from the energy-energy correlator. (DMT, $\chi_{\text{lim}} = 256$, $\tau = 0.5$) The scaling exponent 1.3 yields the best approximate collapse of the corrections, as visually determined at the plotted times.

The oscillatory behavior, together with (27), is consistent between the largest bond dimensions we use and across the smallest Trotter steps we use (Appendix E), and it also appears in the operator size truncated dynamics (Section IV B 3). We do not know if this behavior is generic, coincidental, or a result of some special feature of the mixed-field Ising model; the mechanisms causing these oscillations could be the focus of future work.

The exponential decay of the current extends over almost three decades of magnitude.

This is in tension with the general theoretical expectation that non-linear corrections to hydrodynamics will lead to power-law decay of most hydrodynamic quantities, including the current [32, 45], in the long-time limit. The inset of Fig. 3 shows $\langle J(t)J(0) \rangle$ on a log-log plot with a comparison to the theoretical prediction $\langle J(t)J(0) \rangle \sim t^{-4}$ of 45 for the current decay in a system with one conserved quantity. It is evident that within the time range of our converged numerics, the current decays more rapidly than t^{-4} and has no extended time regime consistent with power law decay. We note that this finding is consistent with the numerical results of 45, which also found decay of the current-current correlator to be faster than theoretical expectations. In the energy-energy correlator, however, we do see power-law corrections to diffusion, as shown in Fig. 5. This is consistent with 45 though the exact exponent is different, possibly due to finite time constraints.

We believe that our convergence testing (Fig. 4) shows true convergence, not a plateau of misleading apparent convergence, because the nonlinearities leading to long-time tails can in principle be captured by DMT. Consider a simple description of long time tails along the

lines of Mukerjee *et al.* in 32.⁵ In that description the total current J is coupled to nonlinear terms like $(\partial_x \varepsilon)^3$ and each of the factors $(\partial_x \varepsilon)$ evolves according to the bare diffusive propagator. So to see the effect of nonlinearities, the MPO must represent a three-point operator $(\partial_x \varepsilon)(\partial_y \varepsilon)(\partial_z \varepsilon)$, together with the operators required to simulate the local evolution of the three factors. At finite time t , all of x, y, z will be within a distance $l \sim t^{1/2}$ of each other, because each $\partial_x \varepsilon$ evolves diffusively. Since the product of three local operators separated by $\lesssim l$ has bond dimension $\chi \propto l$, with the constant set by the complexity of the local operators, we expect that seeing nonlinear corrections to hydrodynamics will require bond dimension $\chi \propto l \sim t^{1/2}$. Because the bond dimension required is polynomial in time, convergence even at moderate bond dimensions (the 256-512 shown in Fig. 4) is good evidence that DMT is accurately capturing even nonlinear corrections to diffusion.

We cannot, however, rule out that power-law behavior with a small coefficient dominates at times longer than those we study here, but the amplitude of any such decay must be small compared to the exponential decay of the current that dominates on the timescales we treat. Indeed the worsening convergence at the end of Fig. 4, for $t \gtrsim 60$ —where we do not consider our simulations converged—might come from a transition to power-law long-time behavior that our moderate bond dimensions do not capture, although other effects may also cause failure of convergence.

B. Method comparison

1. TEBD against TEBD with DMT

Fig. 4 shows how TEBD and DMT simulations converge to the $\chi_{\text{lim}} = 512$ DMT simulations. We measure the relative error

$$\left| 1 - \frac{C_{M, \chi_{\text{lim}}}^{JJ}}{C_{\text{DMT}, 512}^{JJ}} \right|, \quad (28)$$

where

$$C_{M, \chi_{\text{lim}}}^{JJ} = \frac{1}{L} \langle J(t)J(0) \rangle \quad (29)$$

computed with method $M \in \{\text{TEBD}, \text{DMT}\}$ at maximum bond dimension χ_{lim} .

We find that DMT significantly outperforms TEBD at long times ($\gtrsim 50$), even at modest bond dimensions;

⁵ Note that Mukerjee *et al.* [32] consider systems with several conserved quantities n_α , where the leading nonlinearity was $n_\alpha \partial_x n_\beta$. Our system, by contrast, has only one conserved quantity ε , so the leading nonlinearity is $(\partial_x \varepsilon)^3$. We have translated their argument to apply to our model, and rephrased it in terms of operators.

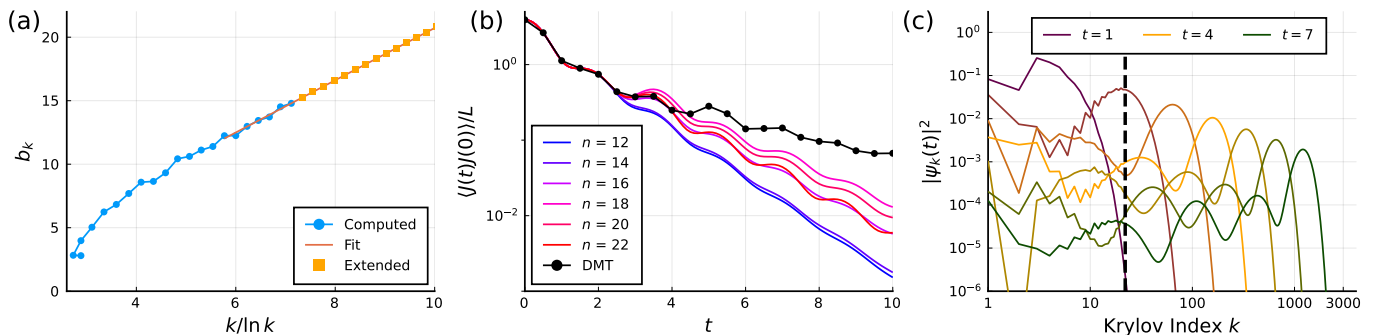


FIG. 6. Recursion method with universal operator growth hypothesis. **(a)**: The first 22 Krylov coefficients b_k plotted against $k/\ln k$, with the linear fit used to extend the series beyond $k = 22$. The fit is computed using b_k for $16 \leq k \leq 22$. **(b)**: Current-current correlator $\langle J(t)J(0) \rangle$ computed using the extended Krylov series, using n exact Krylov coefficients and extended with a fit computed using b_k for $n - 6 \leq k \leq n$. The results do not converge with increasing n , nor do they agree with the converged DMT calculations (even at short times $t \gtrsim 4$). **(c)**: Distribution of operator weight of $J(t)$ in the Krylov basis with $n = 22$ Krylov coefficients computed exactly. After $t_* \sim 2$ the operator has appreciable weight on the artificially extended part of the chain with $k > 22$ (right of black dashed line).

at $t \sim 70$, the DMT results remain converged on the exponential as shown in Fig. 3. Though this time period contributes less to the diffusion coefficient, it is critical in determining the lack of long time tails.

At shorter times ($t \lesssim 20$), DMT performs no better than TEBD. Since this region overwhelmingly determines the diffusion coefficient, we do not expect greater accuracy from DMT in systems without long time tails. Contrarily, systems that do feature long-time tails may require the persisting accuracy of DMT to extract accurate diffusion coefficients.

2. Recursion method with universal operator growth hypothesis

Fig. 6(b) shows the current-current correlation function $\langle J(t)J(0) \rangle$ computed by R-UOG together with DMT simulations. The R-UOG correlator agrees with DMT at short times $t \lesssim 4$, but then departs dramatically. That departure can be delayed only slightly by increasing n , the number of Krylov coefficients computed exactly. (We stop at $n = 22$ because computing Krylov coefficients is exponentially difficult in n).

In Fig. 6(c), we plot the coefficients of $J(t)$ in the Krylov basis, which we label ψ_k , as a function of time; the dashed line marks $k = 22$, the largest Krylov coefficient we compute exactly. The peak of $J(t)$'s distribution crosses $k = 22$ around $t = t_* \sim 2$. The discrepancy between the true coefficients b_k and the universal operator growth hypothesis fit can in principal affect the correlator $\langle J(t)J(0) \rangle$ only after the particle represented by $\psi_k(t)$ has had sufficient time to hop from $k = 1$ to $k = k^*$ and back. In this simulation, this earliest possible time of divergence occurs around $t = 2t_* \sim 4$; Fig. 6 shows that the R-UOG estimate of $\langle J(t)J(0) \rangle$ indeed diverges from the DMT result near this time.

We conclude that R-UOG incorrectly estimates the

current-current correlator $\langle J(t)J(0) \rangle$ because the universal operator growth hypothesis fails to capture important features of the Krylov coefficients. By design, the universal operator growth hypothesis smooths out details (see Fig. 6 left, where we plot the Krylov coefficients for our model). The hypothesis implicitly requires that these details not affect transport coefficients. But the departure visible in the current-current correlator of Fig. 6(b), together with the amplitude distribution of Fig. 6(c), suggest that this is not the case. Assuming that for larger k^* , the R-UOG estimate diverges from the physical value at the earliest possible time $t \sim 2t^*$, we see that capturing the correlator to a desired time t requires computing $k^* \sim \exp(t)$ Krylov coefficients accurately.

3. Operator size truncated dynamics

The operator size truncated (OST) dynamics has two parameters: the operator diameter l_* at which we impose the absorbing boundary, and the loss rate γ at the absorbing boundary. The proper loss rate can be estimated from properties of the Liouvillian graph (as in Eq. 24), but it is instructive to vary γ and probe the sensitivity of the results to that estimate.

In Fig. 7 we show the current-current correlation function at fixed $l_* = 12$, for a variety of γ , together with the converged DMT calculation. The OST dynamics accurately captures the average decay rate of the current-current correlator and the frequency of oscillations about that decay rate. But for some γ the oscillations appear to grow; in the language of the phenomenological three-pole characterization of Eq. 26, those γ show $z_0 > \text{Re } z_1$, though still close to the fine-tuned $|z_0 - \text{Re } z_1| \lesssim 1/70$.

Fig. 8 shows the predicted diffusion coefficient as a function of the loss rate γ . For large l_* , the diffusion coefficient is insensitive to the loss rate γ . This is because (in the language of Eq. 26) the diffusion coefficient is

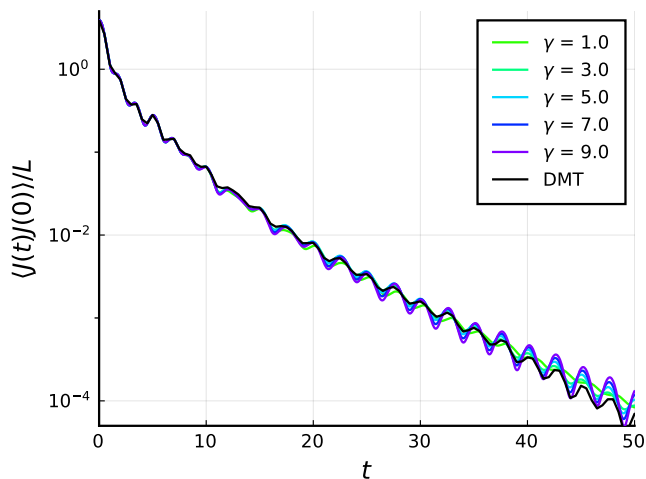


FIG. 7. Current correlator $\langle J(t)J(0) \rangle$, computed using the operator size truncated (OST) dynamics at $l_* = 12$, across absorption rates γ , together with $\chi_{\text{lim}} = 512$ DMT simulations. (The prediction (24) gives $\gamma = 7.01$.) The operator size truncated dynamics matches the overall decay of the correlator, but exaggerates the oscillation.

controlled by the decay rate $z_0 \approx \text{Re } z_1$, which the OST dynamics predicts correctly.

As with DMT, one might worry that the OST dynamics artificially truncate any effects of nonlinear corrections to hydrodynamics. As with DMT, though, we believe that for finite times and polynomially large cutoff diameters, the OST dynamics will in fact capture those nonlinear effects, so convergence testing in l_* (and γ) is a reliable guide to the validity of our simulations. In particular, the OST dynamics keeps arbitrarily high powers of energy density, as long as all of the factors are close to each other (inside the cutoff diameter l_*). Put another way—the OST dynamics should capture that part of the nonlinearity contained inside a diameter l_* and throw away the rest. But for times $\propto l_*^2$ this is enough, because at finite times the relevant operators are separated by a distance $l \propto \sqrt{t}$. Moreover the fact that the OST dynamics agrees with the MPO dynamics, despite truncating different portions of the nonlinearities, gives us confidence that only the local, low-bond dimension nonlinearities captured by both methods are important on the timescales that we treat.

V. SHORT-WAVELENGTH OSCILLATORY MODES: HOT BAND SECOND SOUND

Fig. 9(top) shows the spatial Fourier transform of the energy-energy correlator

$$C^{\varepsilon\varepsilon}(k, t) = \sum_x e^{-ikx} \text{Tr}[\varepsilon_x(t)\varepsilon_0(0)].$$

At small momenta, the correlator displays diffusive behavior (exponential decay with rate Dk^2) with a diffusion

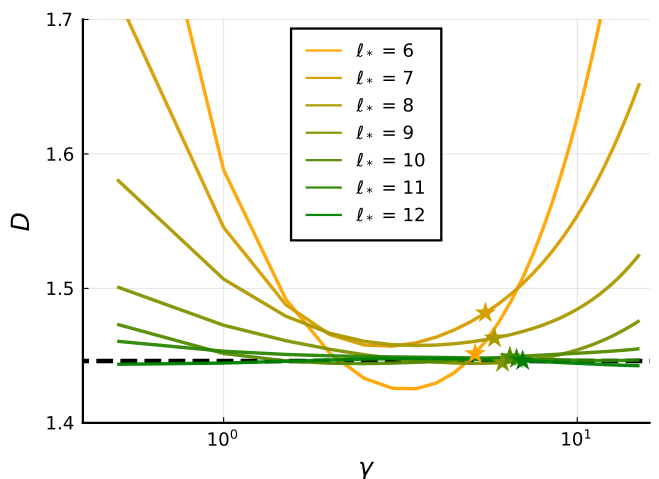


FIG. 8. Diffusion coefficients computed with the OST dynamics as a function of l_* and loss rate γ . Stars denote the semi-empirical value of $\gamma(\ell)$ (24). The dashed line marks the diffusion coefficient computed using DMT. As l_* increases, the prediction becomes increasingly insensitive to the value of γ and converges towards the DMT result.

coefficient D that matches that computed from the integral under the zero-momentum current.

But at larger momenta, we observe underdamped oscillations of the energy-energy correlator; by analogy with 25, we dub these oscillations hot band second sound. The overdamped and underdamped regime can be characterized using a two-pole decay by fitting $C^{\varepsilon\varepsilon}(k, t)$ to the form

$$C^{\varepsilon\varepsilon}(k, t) = A_+ e^{-z_+ t} + A_- e^{-z_- t} \quad (30)$$

where either

$$z_+ = z_-^*, \quad A_+ = A_-^* \quad (31)$$

or

$$z_{\pm}, A_{\pm} \in \mathbb{R}. \quad (32)$$

We see in Fig. 9(top) that this fit largely matches the correlator in both the overdamped and underdamped regime for short times, though it misses some of the oscillatory detail.

Fig. 9(bottom) shows the fit coefficients. At long wavelengths the decay rates are purely real $z \approx Dk^2$ with diffusion coefficient $D \approx 1.446$. But for momenta above a sharp cutoff ($k \approx 0.50$) the Fourier modes $\varepsilon_k(t)$ become oscillatory and the decay coefficients become complex.

We can understand both the small- k diffusive behavior and the oscillatory modes in terms of a microscopic toy model motivated by the structure of the Liouvillian graph. In the Liouvillian graph the energy density is a state $|\varepsilon_x\rangle$ on certain diameter-1 and -2 pools; write its Fourier transform

$$|\varepsilon_k\rangle = \sum_x e^{-ikx} |\varepsilon_x\rangle. \quad (33)$$

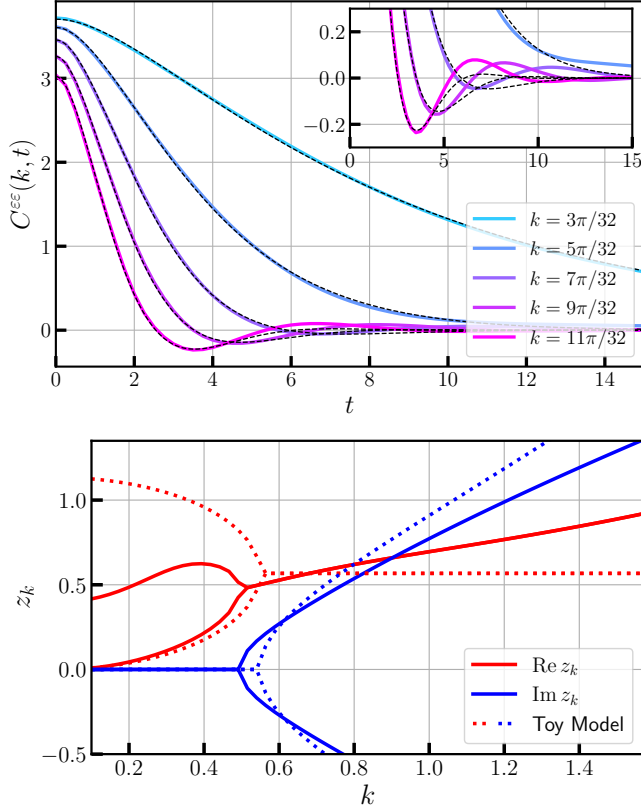


FIG. 9. **Top:** Energy of momentum modes over time, fit with the model in Eq. 30. Data from DMT calculation at $\chi_{\text{lim}} = 512$, $\tau = 0.25$. **Bottom:** The complex decay rates from the fit in Eq. 30. Below a critical wave-vector ($k \approx 0.5$), the exponential decay follows predictable diffusion. Beyond this point, oscillations are present and the quadratic relationship disappears. Results from the toy model (Eq. 40) are shown as dotted lines.

Likewise (for the Ising model (1)) the current operator is a state $|j_x\rangle$ on certain diameter-2 pools; write its Fourier transform

$$|j_k\rangle = \sum_x e^{-ikx} |j_x\rangle. \quad (34)$$

The continuity equation is

$$\partial_t |\varepsilon_k\rangle = 2i \sin(k/2) |j_k\rangle. \quad (35)$$

In terms of orthonormal operators $|\hat{\varepsilon}_k\rangle = |\varepsilon_k\rangle (\text{Tr } \varepsilon_k^\dagger \varepsilon_k)^{-1/2}$ and $|\hat{j}_k\rangle = |j_k\rangle (\text{Tr } j_k^\dagger j_k)^{-1/2}$, the continuity equation becomes a term in an effective Liouvillian

$$\sum_k 2a_k \sin(k/2) |\hat{\varepsilon}_k\rangle \langle \hat{j}_k| + \text{h.c.} \quad (36)$$

with

$$a_k^2 = \frac{\text{Tr } j_k^\dagger j_k}{\text{Tr } \varepsilon_k^\dagger \varepsilon_k} = \frac{2g_x^2}{1 + (g_x^2 + g_z^2) \cos^2(k/2)}. \quad (37)$$

Note that in this section, we use the caret to denote a normalized vector as opposed to an operator.

Additionally, weight from each current operator decays into the set of larger-diameter operators. In the spirit of the OST effective model of Section III C, mock this up by a uniform non-Hermitian decay $-i\Gamma \sum_k |\hat{j}_k\rangle \langle \hat{j}_k|$. The toy model Liouvillian is then

$$\mathcal{L}_{\text{toy}} = \sum_k \left[2a_k \sin(k/2) |\hat{\varepsilon}_k\rangle \langle \hat{j}_k| + \text{h.c.} - i\Gamma |\hat{j}_k\rangle \langle \hat{j}_k| \right]. \quad (38)$$

This Liouvillian gives an exact exponential decay $\langle J(t)J(0) \rangle \propto e^{-\Gamma t}$, because the total current $J = j_{k=0}$ is an eigenstate of \mathcal{L}_{toy} with eigenvalue $-i\Gamma$.

In terms of the memory matrix formalism [33, 42, 43] (see 9 and 47 for more recent discussions), the toy model (38) replaces the memory matrix $M_{\varepsilon\varepsilon}(z)$ with a single decay rate Γ . We give an elementary, largely self-contained discussion of the memory matrix and the connection between finite momentum and $k = 0$ dynamics in Appendix F. The toy model is also formally equivalent to the hydrodynamics with finite current relaxation rate of 1.

Upon diagonalization the toy Liouvillian becomes

$$\mathcal{L}_{\text{toy}} = \sum_{n\zeta} (-iz_{k\zeta}) f_{k\zeta}^\dagger f_{k\zeta}, \quad (39)$$

where k is the momentum, $\zeta = \pm 1$ labels the two modes at each momentum, $f_{k\zeta}^\dagger$ ($f_{k\zeta}$) are creation (annihilation) operators for the modes at momentum k , and

$$z_{k\zeta} = \frac{\Gamma}{2} \left(1 + \zeta \sqrt{1 - \left(\frac{4a_k}{\Gamma} \sin(k/2) \right)^2} \right) \quad (40)$$

are the decay rates of the two modes.⁶ For small k the $\zeta = -1$ decay rate, corresponding to the energy density, is $z_k = -(a_0^2/\Gamma) k^2$, allowing us to connect the diffusion coefficient to the decay rate:

$$\Gamma = a_0^2/D \quad (41)$$

We can recover the same expression by integrating the exponential decay of the current-current operator and using Eq. 12b.

Fig. 9(bottom) shows decay rates from DMT together with the predictions of the toy model. The toy model has a single free parameter Γ ; we set Γ using the diffusion

⁶ At finite k , these decay rates are dependent on our definition of the energy density. Had we chosen a different energy density—e.g. $\varepsilon_x = 4S_x^z S_{x+1}^z + 2g_x S_x^x + 2g_z S_x^z$, which is not parity symmetric—we would have found a different normalization $\text{Tr } \varepsilon_k^\dagger \varepsilon_k$, hence a different a_k and a different set of decay rates. The decay rates would match at small k .

coefficient $D = 1.446$ and (41). The toy model predicts an exceptional point—a transition from overdamped to underdamped—at $k \approx 0.55$, compared to $k \approx 0.5$ in fits to DMT data. For $k < k_c$ both modes have real decay, with $\zeta = -1$ slower; for $k > k_c$ the two modes have the same decay, while the decay rate $z_{k\zeta}$ develops an imaginary component. Physically this means that for long wavelength the slow modes are “overdamped,” and display no oscillations, while for short wavelength the slow modes are “underdamped,” leading to oscillations.

The toy model quantitatively predicts the finite-wavelength dynamics in the sense that it gives an exceptional point k_c within about 10% of the DMT fits, even though its only free parameter was set using behavior in the long-wavelength diffusive limit.

Although the toy model matches the behavior of the slowest-decaying mode, it also gives a prediction for the other mode ($\zeta = +1$) that does not match the DMT data below the critical k_c . We speculate that the discrepancy comes from the additional, nontrivial structure in the current decay. In the language of Sec. F, one arrives at the toy model by replacing the complex dynamics of the current (i.e. the superoperator M_k in (F5)) by a simple exponential decay with rate Γ . Such a single decay captures only gross, short-time features of the current-current correlator $\langle J(t)J(0) \rangle$ shown in Figs. 3 and 7. In particular, while the toy model predicts a single decay rate, Figs. 3 and 7 shows at least two (a fast early decay for $t \lesssim 20$ and a slow long-time decay), and the toy model does not predict the oscillations visible in Figs. 3 and 7. Moreover, the asymptotic decay rate of the correlator $\langle J(t)J(0) \rangle$ is slower than the value of Γ estimated here. The true $\zeta = +1$ decay rate may result from structure ignored by that simple approximation. It is not clear what particular structure results in the small- k discrepancy between toy model and DMT data; the relevant discrepancy maybe related to nonlinear corrections to the hydrodynamic description.

We do not claim that the toy model reflects the true long-time behavior of the system, since we only compare to correlators over a short time; at finite k , longer times become difficult to properly fit.

VI. CONCLUSION

We have simulated the hydrodynamics of the fruit-fly one-dimensional (1D) nonintegrable Hamiltonian, i.e., the Ising model with tilted onsite field, using four numerical methods: TEBD [21, 23], TEBD with density matrix truncation (DMT) [16], the recursion method with universal operator growth hypothesis (R-UOG) [19, 38], and operator size truncated (OST) dynamics [20]. The universal operator growth hypothesis and the truncated Liouvillian graph methods both rely on assumptions about the dynamics of operators on the system: R-UOG relies on an ansatz for the Lanczos coefficients of the operator dynamics and OST relies on a chaos assumption about

the dynamics of large-diameter operators. Both assumptions require that the long-operator dynamics be unstructured. TEBD with SVD truncation makes no such assumption—at each timestep, the SVD truncation gives a low-bond-dimension MPO that is close in Frobenius norm—but by the same token offers no guarantee that the local operators known to be important for hydrodynamics are preserved. DMT, by contrast, imports locality into the truncation by optimizing the L^2 norm subject to the constraint that local operators be unchanged. This truncation is appropriate for a wide range of systems; it has been successfully used for thermalizing [16, 48] and Bethe ansatz integrable [2, 49] systems. We found that DMT gives converged current-current correlators to times $t \approx 60$ with bond dimension 256, while TEBD fails to converge for times $t \gtrsim 20$; we also gave heuristic arguments that nonlinear hydrodynamics requires polynomial bond dimension, putting our convergence testing on firmer conceptual ground. We found that the converged current-current correlators show exponential decay for the times we treat; suggesting that the coefficients of power-law long time tails—if they exist—are small enough that the tails are dominated by the exponential decay for $t \lesssim 60$.

We then used the converged DMT simulations to check the operator-size truncated (OST) dynamics and the recursion method with universal operator growth hypothesis (R-UOG). We found that the OST dynamics matches the overall decay of the current-current correlator and gives accurate diffusion coefficients. Indeed, although certain curious long-time oscillatory features of the correlator are sensitive to the choice of the artificial decay γ , the diffusion coefficient is increasingly insensitive to γ as the length scale l^* is increased. This agreement suggests that the underlying assumption of the OST dynamics—that the dynamics of long operators is chaotic and can be modelled by a simple decay—accurately reflects the portion of the dynamics that is important to transport.

The recursion method with universal operator growth hypothesis (R-UOG), by contrast, gives current-current correlators that depart from DMT simulations at $t \approx 4$, as soon as the operator growth hypothesis becomes operative. The R-UOG simulations also do not converge at feasible a Krylov index. The universal operator growth hypothesis intentionally discards details of long-operator dynamics, as do all of the methods considered here. We cannot rule out that R-UOG begins to converge for Krylov order $n \gtrsim 22$, beyond our calculations. In particular, if we take enough Krylov coefficients to reach the regime described by the phenomenological three-pole model (26), the R-UOG may converge. But its failure to capture the current-current correlator (and consequently the diffusion coefficient) at the Krylov order that we treat here suggests that the details it discards are important to transport.

We then computed a momentum-dependent energy density dynamical correlation function. This correlation function displays a crossover from long-wavelength dif-

fusive behavior to short-wavelength oscillatory behavior, which we dub “hot band second sound” by analogy with the hot band sound of 25. We explained this hot band second sound with a toy model rooted in the OST dynamics. The toy model has a single free parameter, a current decay rate, which we set using the long-wavelength diffusion coefficient; even so, it quantitatively predicts the onset of oscillations.

Our results underscore that diffusion is largely controlled by short-time behavior, so it does not sensitively test how well a method can capture long-time dynamics. Because the asymptotic value of the diffusion coefficient is $D = \int_0^\infty dt' \langle J(t)J(0) \rangle$, it is dominated by early-time contributions when the current-current correlator is large. (This is all the more true when—as we found—the current-current correlator decays exponentially.) Consequently even methods that fail to converge at later times can still produce approximately correct values for the diffusion coefficient. TEBD, for example, produces a diffusion coefficient within 1% of the DMT and OST values, even though it fails to converge for $t \gtrsim 20$. We expect similar behavior even when the diffusion coefficient is computed using some other correlator, e.g. the energy density correlator $C^{\epsilon\epsilon}(x, t)$: as long as the method gives approximately diffusive dynamics, the diffusion coefficient will be linked to the current-current correlator by a series of identities. Reproducing a dynamical correlator such as $\langle J(t)J(0) \rangle$ is a more sensitive test of how well a method approximates a system’s dynamics. As DMT and the OST dynamics yield converged results for

dynamical correlators over a long time interval, we expect that these methods will be useful for studying dynamics in many similar systems.

ACKNOWLEDGMENTS

We are grateful for helpful conversations with Brian Swingle, Mike Winer, Peter Lunts, and Alex Schuckert. SYT thanks the Joint Quantum Institute at the University of Maryland for support through a JQI fellowship. This research was performed while BW held an NRC postdoctoral fellowship at the National Institute of Standards and Technology. BW was supported in part by the DoE ASCR Accelerated Research in Quantum Computing program (award No. DE-SC0020312). C.D.W. was supported by the U.S. Department of Energy (DOE), Office of Science, Office of Advanced Scientific Computing Research (ASCR) Quantum Computing Application Teams program, under fieldwork proposal number ERKJ347, DOE Quantum Systems Accelerator program DE-AC02-05CH11231, AFOSR MURI FA9550-22-1-0339, ARO grant W911NF-23-1-0242, ARO grant W911NF-23-1-0258, and NSF QLCI grant OMA-2120757. JS acknowledges support from the Joint Quantum Institute. This work is also supported by the Laboratory for Physical Sciences through its continuous support of the Condensed Matter Theory Center at the University of Maryland.

-
- [1] P. T. Brown, D. Mitra, E. Guardado-Sanchez, R. Nourafkan, A. Reymbaut, C.-D. Hébert, S. Bergeron, A.-M. S. Tremblay, J. Kokalj, D. A. Huse, P. Schauf, and W. S. Bakr, Bad metallic transport in a cold atom fermi-hubbard system, *Science* **363**, 379 (2019).
- [2] D. Wei, A. Rubio-Abadal, B. Ye, F. Machado, J. Kemp, K. Srakaew, S. Hollerith, J. Rui, S. Gopalakrishnan, N. Y. Yao, I. Bloch, and J. Zeiher, Quantum gas microscopy of kardar-parisi-zhang superdiffusion, *Science* **376**, 716 (2022).
- [3] J. Zaanen, Planckian dissipation, minimal viscosity and the transport in cuprate strange metals, *SciPost Physics* **6**, 061 (2019).
- [4] J. Ayres, M. Berben, M. Čulo, Y.-T. Hsu, E. van Heumen, Y. Huang, J. Zaanen, T. Kondo, T. Takeuchi, J. Cooper, *et al.*, Incoherent transport across the strange-metal regime of overdoped cuprates, *Nature* **595**, 661 (2021).
- [5] N. R. Poniatowski, T. Sarkar, R. P. S. M. Lobo, S. Das Sarma, and R. L. Greene, Counterexample to the conjectured planckian bound on transport, *Physical Review B* **104**, 235138 (2021).
- [6] B. Spivak, S. V. Kravchenko, S. A. Kivelson, and X. P. A. Gao, Colloquium: Transport in strongly correlated two dimensional electron fluids, *Reviews of modern physics* **82**, 1743 (2010).
- [7] S. Kasahara, T. Shibauchi, K. Hashimoto, K. Ikada, S. Tonegawa, R. Okazaki, H. Shishido, H. Ikeda, H. Takeya, K. Hirata, *et al.*, Evolution from non-fermi to fermi-liquid transport via isovalent doping in bafe 2 (as 1- x p x) 2 superconductors, *Physical Review B* **81**, 184519 (2010).
- [8] S. Sachdev and B. Keimer, Quantum criticality, *Physics Today* **64**, 29 (2011).
- [9] A. Lucas and S. Sachdev, Memory matrix theory of magnetotransport in strange metals, *Physical Review B* **91**, 195122 (2015).
- [10] M. Stephanov, K. Rajagopal, and E. Shuryak, Signatures of the tricritical point in QCD, *Physical Review Letters* **81**, 4816 (1998).
- [11] P. F. Kolb, J. Sollfrank, and U. Heinz, Anisotropic transverse flow and the quark-hadron phase transition, *Physical Review C* **62**, 054909 (2000).
- [12] J.-Y. Ollitrault, Anisotropy as a signature of transverse collective flow, *Phys. Rev. D* **46**, 229 (1992).
- [13] STAR Collaboration, An Experimental Exploration of the QCD Phase Diagram: The Search for the Critical Point and the Onset of De-confinement, arXiv:1007.2613 [nucl-ex] (2010).
- [14] U. Heinz, P. Sorensen, A. Deshpande, C. Gagliardi, F. Karsch, T. Lappi, Z.-E. Meziani, R. Milner, B. Muller, J. Nagle, J.-W. Qiu, K. Rajagopal, G. Roland, and R. Venugopalan, Exploring the properties of the phases of QCD matter - research opportunities and priorities for

- the next decade, arXiv:1501.06477 [hep-ex, physics:hep-ph, physics:nucl-ex, physics:nucl-th] (2015).
- [15] C. von Keyserlingk, F. Pollmann, and T. Rakovszky, Operator backflow and the classical simulation of quantum transport, *Physical Review B* **105**, 245101 (2022).
- [16] C. D. White, M. Zaletel, R. S. K. Mong, and G. Refael, Quantum dynamics of thermalizing systems, *Physical Review B* **97**, 035127 (2018).
- [17] T. Rakovszky, C. W. von Keyserlingk, and F. Pollmann, Dissipation-assisted operator evolution method for capturing hydrodynamic transport, *Physical Review B* **105**, 075131 (2022).
- [18] T. K. Kvorning, L. Herviou, and J. H. Bardarson, Time-evolution of local information: thermalization dynamics of local observables, *SciPost Phys.* **13**, 080 (2022).
- [19] D. E. Parker, X. Cao, A. Avdoshkin, T. Scaffidi, and E. Altman, A universal operator growth hypothesis, *Physical Review X* **9**, 041017 (2019).
- [20] C. D. White, Effective dissipation rate in a liouvillian-graph picture of high-temperature quantum hydrodynamics, *Physical Review B* **107**, 094311 (2023).
- [21] G. Vidal, Efficient classical simulation of slightly entangled quantum computations, *Physical Review Letters* **91**, 147902 (2003).
- [22] G. Vidal, Efficient simulation of one-dimensional quantum many-body systems, *Physical Review Letters* **93**, 040502 (2004).
- [23] M. Zwolak and G. Vidal, Mixed-state dynamics in one-dimensional quantum lattice systems: A time-dependent superoperator renormalization algorithm, *Physical Review Letters* **93**, 207205 (2004).
- [24] E. Leviatan, F. Pollmann, J. H. Bardarson, D. A. Huse, and E. Altman, Quantum thermalization dynamics with Matrix-Product States, arXiv:1702.08894 [cond-mat, physics:quant-ph] (2017), arxiv:1702.08894 [cond-mat, physics:quant-ph].
- [25] V. B. Bulchandani and D. A. Huse, Hot band sound (2022), arXiv:2208.13767.
- [26] H. Kim and D. A. Huse, Ballistic spreading of entanglement in a diffusive nonintegrable system, *Physical Review Letters* **111**, 127205 (2013).
- [27] H. Kim, T. N. Ikeda, and D. A. Huse, Testing whether all eigenstates obey the eigenstate thermalization hypothesis, *Physical Review E* **90**, 052105 (2014).
- [28] L. D. Landau and E. M. Lifshitz, *Fluid Mechanics: Landau and Lifshitz: Course of Theoretical Physics, Volume 6*, Vol. 6 (Elsevier, 2013).
- [29] B. Doyon, Lecture notes on Generalised Hydrodynamics, *SciPost Physics Lecture Notes*, 018 (2020).
- [30] J. D. Nardis and B. Doyon, Hydrodynamic gauge fixing and higher order hydrodynamic expansion, *Journal of Physics A: Mathematical and Theoretical* **56**, 245001 (2023).
- [31] R. Steinigeweg, H. Wichterich, and J. Gemmer, Density dynamics from current auto-correlations at finite time- and length-scales, *EPL (Europhysics Letters)* **88**, 10004 (2009).
- [32] S. Mukerjee, V. Oganesyan, and D. Huse, Statistical theory of transport by strongly interacting lattice fermions, *Physical Review B* **73**, 035113 (2006).
- [33] D. Forster, *Hydrodynamic fluctuations, broken symmetry, and correlation functions*, *Frontiers in physics*; 47 (W.A. Benjamin, Advanced Book Program, Reading, Mass., 1975).
- [34] S. Hild, T. Fukuhara, P. Schauss, J. Zeiher, M. Knap, E. Demler, I. Bloch, and C. Gross, Far-from-equilibrium spin transport in heisenberg quantum magnets, *Physical Review Letters* **113**, 147205 (2014).
- [35] U. Schollwöck, The density-matrix renormalization group in the age of matrix product states, *Annals of Physics* **326**, 96 (2011).
- [36] T. Barthel and Y. Zhang, Optimized lie-trotter-suzuki decompositions for two and three non-commuting terms, *Annals of Physics* **418**, 168165 (2020).
- [37] D. C. Mattis, How to reduce practically any problem to one dimension, in *Springer Series in Solid-State Sciences* (Springer Berlin Heidelberg, 1981) pp. 3–10.
- [38] V. S. Viswanath and G. Müller, *The Recursion Method* (Springer Berlin Heidelberg, 1994).
- [39] E. Altman, Computing quantum thermalization dynamics (2018).
- [40] P. Ehrenfest and T. Ehrenfest, *The Conceptual Foundations of the Statistical Approach in Mechanics* (Dover Publications, 2002).
- [41] G. A. Gottwald and M. Oliver, Boltzmann's dilemma: An introduction to statistical mechanics via the kac ring, *SIAM Review* **51**, 613 (2009).
- [42] R. Zwanzig, Memory effects in irreversible thermodynamics, *Physical Review* **124**, 983 (1961).
- [43] H. Mori, Transport, collective motion, and brownian motion, *Progress of Theoretical Physics* **33**, 423 (1965).
- [44] J. Haegeman, *Krylovkit* (2024).
- [45] A. A. Michailidis, D. A. Abanin, and L. V. Delacrétaz, Corrections to diffusion in interacting quantum systems, *Phys. Rev. X* **14**, 031020 (2024).
- [46] P. Virtanen, R. Gommers, T. E. Oliphant, M. Haberland, T. Reddy, D. Cournapeau, E. Burovski, P. Peterson, W. Weckesser, J. Bright, S. J. van der Walt, M. Brett, J. Wilson, K. J. Millman, N. Mayorov, A. R. J. Nelson, E. Jones, R. Kern, E. Larson, C. J. Carey, Í. Polat, Y. Feng, E. W. Moore, J. VanderPlas, D. Laxalde, J. Perktold, R. Cimrman, I. Henriksen, E. A. Quintero, C. R. Harris, A. M. Archibald, A. H. Ribeiro, F. Pedregosa, P. van Mulbregt, and SciPy 1.0 Contributors, *SciPy 1.0: Fundamental Algorithms for Scientific Computing in Python*, *Nature Methods* **17**, 261 (2020).
- [47] P. Jung and A. Rosch, Lower bounds for the conductivities of correlated quantum systems, *Physical Review B* **75**, 245104 (2007).
- [48] B. Ye, F. Machado, C. D. White, R. S. K. Mong, and N. Y. Yao, Emergent hydrodynamics in nonequilibrium quantum systems, *Physical Review Letters* **125**, 030601 (2020).
- [49] B. Ye, F. Machado, J. Kemp, R. B. Hutson, and N. Y. Yao, Universal kardar-parisi-zhang dynamics in integrable quantum systems, *Phys. Rev. Lett.* **129**, 230602 (2022).
- [50] T. Barthel, Precise evaluation of thermal response functions by optimized density matrix renormalization group schemes, *New Journal of Physics* **15**, 073010 (2013).

Appendix A: Comparison of correlators for $D(t)$ calculation

The time-dependent diffusion constant can be computed using multiple equivalent formulations relying on

different time-dependent correlators: the energy-energy correlator, through Eq. 11, the current-current correlator, through Eq. 12a, and the energy-current correlator. Here we give a general derivation of this connection assuming spatial- and time-translation invariance. We use the charge n instead of the energy for greater generality.

The time-dependent diffusion constant is defined as

$$D(t) = \frac{1}{2\nu} \frac{\partial}{\partial t} \int dx x^2 \langle n(x, t) n(0, 0) \rangle \quad (\text{A1})$$

where $\nu = \langle n(x, t) n(x, t) \rangle$. Bringing the time derivative under the integral and using the conservation law gives

$$D(t) = \frac{1}{2\nu} \int dx x^2 \langle \dot{n}(x, t) n(0, 0) \rangle \quad (\text{A2})$$

$$= -\frac{1}{2\nu} \int dx x^2 \langle \nabla j(x, t) n(0, 0) \rangle. \quad (\text{A3})$$

The resultant spatial derivative cancels out a factor of x through integration by parts:

$$D(t) = -\frac{1}{2\nu} \int dx x^2 \nabla \langle j(x, t) n(0, 0) \rangle \quad (\text{A4})$$

$$= \frac{1}{\nu} \int dx x \langle j(x, t) n(0, 0) \rangle. \quad (\text{A5})$$

This expression gives the time-dependent diffusion constant in terms of the charge-current correlator.

Applying this process again yields the current-current correlator. First, by spatial- and time-translation invariance, the charge-current correlator is equivalent to

$$D(t) = \frac{1}{\nu} \int dx x \langle j(0, 0) n(-x, -t) \rangle. \quad (\text{A6})$$

which by the same procedure gives

$$D(t) = \frac{1}{\nu} \int_0^t dt' \frac{d}{dt'} \int dx x \langle j(0, 0) n(-x, -t') \rangle \quad (\text{A7})$$

$$= \frac{1}{\nu} \int_0^t dt' \int dx \langle j(x, t) j(0, 0) \rangle \quad (\text{A8})$$

$$= \frac{1}{\nu L} \int_0^t dt' \langle J(x, t) J(0, 0) \rangle. \quad (\text{A9})$$

Using a DMT simulation, we calculate $D(t)$ using all three of these values and plot the generally consistent results in Fig. 10. We consider $\langle jj \rangle$ in the rest of the paper in large part because it appears the best converged.

Appendix B: Numerical Convergence in Trotter Step Size

We recreate the current-current decay results (Fig. 3) for various Trotter step sizes τ to demonstrate convergence. The results are shown in Fig. 11. Due to the specific Trotter algorithm used in this study (see Section III A 1), we expect the error from each step to be $O(\tau^4)$ however, for long times these errors accumulate. We numerically find that all values up to $\tau = 0.5$ are convergent at times $t \gtrsim 40$.

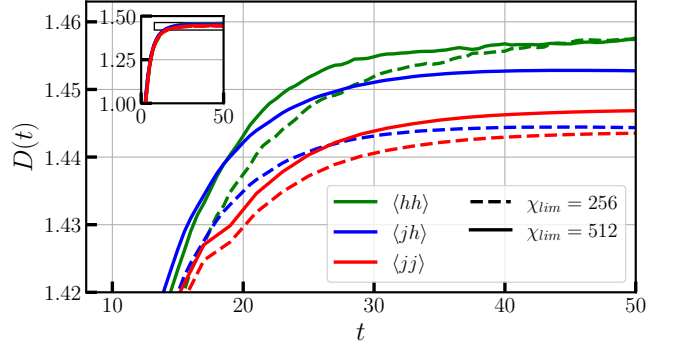


FIG. 10. Comparison of time-dependent diffusion constant calculated using various correlators. Inset shows zoomed-out plot.

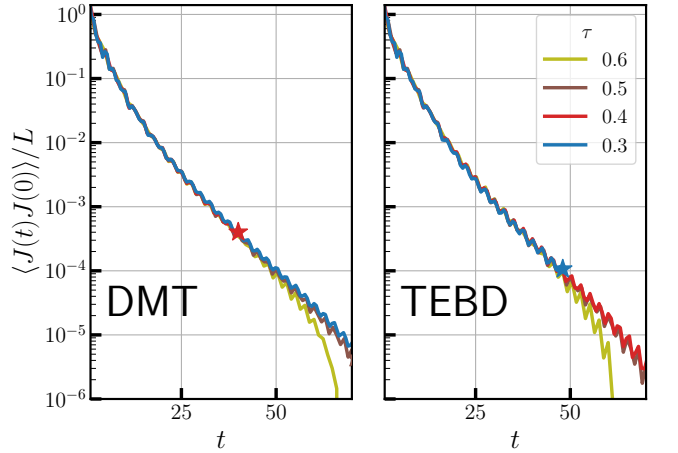


FIG. 11. Current-current correlator decay for different Trotter step sizes τ using time-doubling. $\chi_{\text{lim}} = 512$. Stars mark the end of execution.

Appendix C: Time-Doubling

As described in Section III A, we use MPO methods to calculate the time-dependent operator $j_0(t) = e^{-iHt} j_0 e^{iHt}$ which relates to the current-current Green's function $\langle j_x(t) j_0(0) \rangle$ via Eq. 12a. However under certain conditions—unitary evolution, infinite temperature, time translation invariance and spatial translation invariance—we can use a time-doubling trick [50] to effectively calculate $\langle j_x(2t) j_0(0) \rangle$ from the same MPO calculation.

To demonstrate this procedure, we rewrite the correlator as two time-evolved operators

$$\langle j_x(2t) j_0(0) \rangle = \langle j_x(t) j_0(-t) \rangle. \quad (\text{C1})$$

We calculate the first operator $j_x(t)$ by applying time-inversion and spatial translation onto the MPO $j_0(-t)$. Time inversion acts on the current operator as the complex conjugate, giving

$$j_x(t) = -\hat{T}(x) j_0^*(-t) \hat{T}(-x). \quad (\text{C2})$$

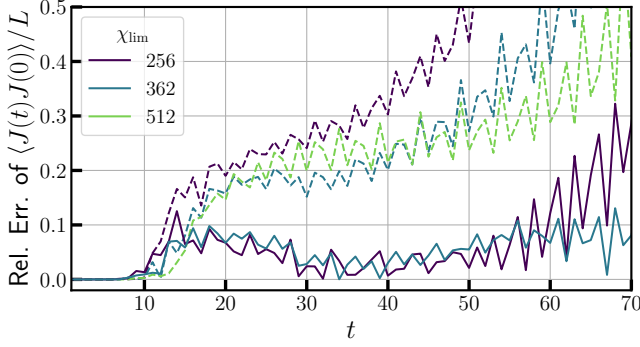


FIG. 12. Unsmoothed relative error in current-current correlator, computed by DMT (solid lines) and TEBD (dashed lines). See Fig. 4 for smoothed data and discussion.

We use this approach in calculating the long-time portions of the MPO results.

Appendix D: DMT for traceless operators

1. As described in 16

DMT as described in 16 truncates a density matrix without modifying any 3-site reduced density matrix. Consider truncation of a matrix product operator $A(t)$ on a bond j (separating sites $j, j+1$). First, DMT as described in 16 uses a gauge transformation to form a correlation matrix

$$M_{\alpha\beta} = \text{Tr} [A(t)\hat{y}_{L\alpha}\hat{y}_{R\beta}], \quad 0 \leq \alpha, \beta \leq \chi - 1.$$

χ is the bond dimension of the matrix product operator $A(t)$, and $y_{L\alpha}, y_{R\beta}$ span the left and right Schmidt spaces at bond j , respectively. The matrix M serves as an orthogonality center: the matrix product operator $A(t)$ can be written

$$A(t) = \left[\begin{array}{|c|c|c|c|} \hline & & & \\ \hline & & \boxed{M} & \\ \hline & & & \\ \hline \end{array} \right] \quad (\text{D1})$$

where $\left[\begin{array}{|c|c|c|c|} \hline & & & \\ \hline & & & \\ \hline & & & \\ \hline \end{array} \right]$ and $\left[\begin{array}{|c|c|c|c|} \hline & & & \\ \hline & & & \\ \hline & & & \\ \hline \end{array} \right]$ are left- and right-canonical, respectively. The rank of this matrix M therefore controls the bond dimension of the MPO, and the MPO can be truncated by truncating the correlation matrix.

The gauge transformation giving the matrix $M_{\alpha\beta}$ is chosen so that the operators $\hat{y}_{L,\alpha}$ and $\hat{y}_{R,\beta}$ satisfy the following properties:

1. $\hat{y}_{L,\alpha}, \hat{y}_{R,\beta}$ are traceless for $\alpha, \beta > 0$
2. $\hat{y}_{L,\alpha}, \hat{y}_{R,\beta}$ are supported on sites $1, \dots, j$ and $j+1, \dots, L$
3. The image of $\hat{\sigma}_j^\mu$ in the bond space at bond j is spanned by $\{\hat{y}_{L\alpha} : \alpha = 0, \dots, 3\}$, i.e.

$$\text{Tr} [\hat{\sigma}_j^\mu \hat{y}_{L\alpha}] = 0, \quad 4 \leq \alpha \quad (\text{D2})$$

and likewise the image of $\hat{\sigma}_{j+1}^\mu$ in the bond space at bond j is spanned by $\{\hat{y}_{R\beta} : \beta = 0, \dots, 3\}$, i.e.

$$\text{Tr} [\hat{\sigma}_{j+1}^\mu \hat{y}_{R\beta}] = 0, \quad 4 \leq \beta. \quad (\text{D3})$$

When the operator being truncated is a density matrix, these properties of the $\hat{y}_{L,R}$ link the block structure of the matrix $M_{\alpha\beta}$ to local reduced density matrices: one can check that modifications to $M_{\alpha,\beta}$ for $\alpha, \beta \geq 4$ do not change any three-site correlation functions. When the operator being truncated is not a density matrix, the quantities preserved are no longer reduced density matrices, but partial traces of the operator in question.

As described in 16, DMT first forms the matrix of connected components

$$\tilde{M}_{\alpha\beta} = \langle \hat{y}_{L\alpha} \hat{y}_{R\beta} \rangle - \langle \hat{y}_{L\alpha} \rangle \langle \hat{y}_{R\beta} \rangle \quad (\text{D4a})$$

$$= M_{\alpha\beta} - \frac{M_{\alpha 0} M_{0\beta}}{M_{00}}. \quad (\text{D4b})$$

It then truncates the submatrix $\tilde{M}_{\alpha\beta}|_{4 \leq \alpha, \beta}$ by keeping leading principle components for a new matrix of connected components

$$\tilde{M}' = \left[\begin{array}{c|c} & \\ \hline & XrP(\chi)V \\ \hline \end{array} \right]. \quad (\text{D5})$$

Finally it reassembles a new correlation matrix

$$M'_{\alpha\beta} = \tilde{M}'_{\alpha\beta} + \frac{M_{\alpha 0} M_{0\beta}}{M_{00}}. \quad (\text{D6})$$

from the truncated matrix \tilde{M}' and the unchanged column and row $M_{\alpha 0}, M_{0\beta}$.

2. As modified for Heisenberg dynamics and used in this work

Now consider Heisenberg evolution of a traceless operator A . In constructing the matrix of connected components (D4b), the protocol of Sec. D 1 divides by the matrix element M_{00} . When the operator being truncated is a density matrix, the matrix element M_{00} encodes the trace of the density matrix. But we are no longer evolving a density matrix: we are evolving a traceless operator A , so dividing by M_{00} is not natural.

Instead we truncate the matrix M directly. We use the same gauge transformation as in Appendix D 1 and 16, leading to operators $\hat{y}_{L\alpha}, \hat{y}_{R\alpha}$ with the same properties. The matrix

$$M_{\alpha\beta} = \text{Tr} [A\hat{y}_{L\alpha}\hat{y}_{R\beta}] \quad (\text{D7})$$

has a block structure analogous to that of the $M_{\alpha\beta}$ of (D1); in particular, modifications to $M_{\alpha\beta}$ for $\alpha, \beta \geq 4$ do

not change the action of A on any connected three-site region.

But now, instead of forming the matrix of connected components \tilde{M} and truncating that, we directly truncate the matrix M for

$$M' = \left[\begin{array}{c|c} & \\ \hline & XrP(x')V \\ \hline & \end{array} \right]. \quad (\text{D8})$$

Appendix E: Additional convergence data

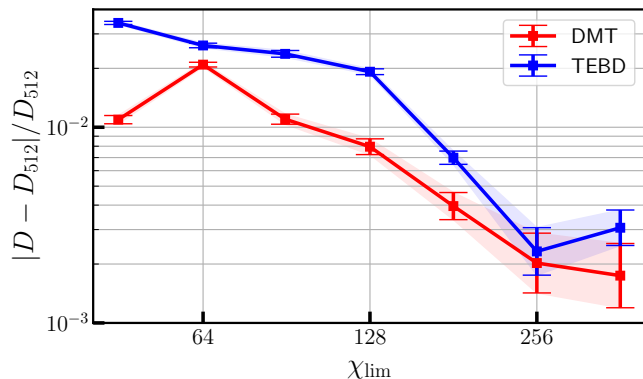


FIG. 13. Convergence of the diffusion coefficient with DMT and TEBD, calculated using $n = 9$ Newton-Coates formula. Fine-grained integration ($\tau = 0.1$) was performed up to $t = 18$ with coarse grained ($\tau = 0.5$) used afterwards. Errors are calculated by doubling the time step.

We analyzed the convergence of the current-current correlator across time by comparing the results of the TEBD and DMT calculations with the largest bond dimension ($\chi_{\text{lim}} = 512$) DMT data. In the main text, Fig. 4 contains data which is smoothed with a Savitzky-Gavoy filter. The corresponding unsmoothed data are shown here in Fig. 12. In each data series, the current exponentially decays with rates that are nearly the same and contains additional oscillatory modes that decay at a similar rate, as in Eq. 26. The oscillatory part of the error is largely due to a mismatch in the amplitude and phase of the oscillations.

Additionally, we analyzed the convergence of the diffusion coefficient computed from the current-current correlator. Fig. 13 shows the results for the diffusion coefficient computed with TEBD and DMT and various bond dimensions, subtracted from the result with the largest bond dimension DMT data. Roughly, the plot shows exponential improvement in the accuracy of the diffusion coefficient with increasing bond dimension; however, the pattern is not consistent enough to be conclusive.

Finally, we analyzed the convergence of the diffusion coefficient within the OST dynamics. Fig. 14 shows the

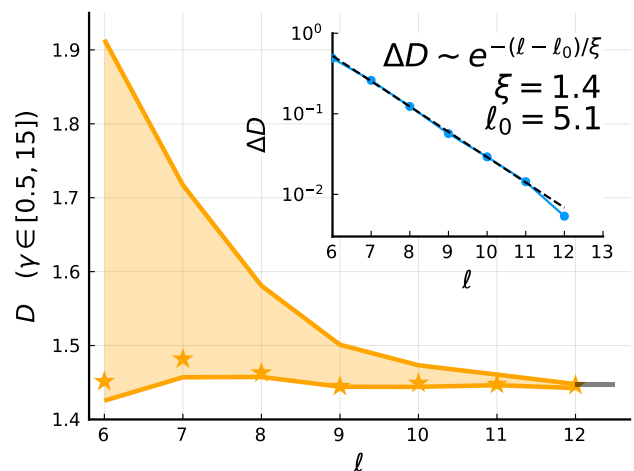


FIG. 14. Maximum and minimum computed values of the diffusion coefficient in the OST dynamics for the range of γ considered, $\gamma \in [0.5, 15]$. The maximum and minimum both converge to the DMT-computed value (denoted with a black mark) as l is increased. For small l , the diffusion coefficient computed with $\gamma_{\text{semi-emp.}}$ (stars) is a good estimate. (Inset) The difference between the maximum and minimum D over this interval of γ shrinks exponentially in l , illustrating the exponentially increased insensitivity of $D(\gamma)$ to the noise rate γ .

range of predicted values for the diffusion coefficient when the absorption rate γ is tuned across the entire range considered, $\gamma \in [0.5, 15]$. The size of this range shrinks exponentially with increasing l , and moreover converges onto the value computed using DMT calculations.

Appendix F: Diffusion and the spectrum of the Liouvillian

In Sec. IIB we related the diffusion coefficient to the time integral of the current-current correlator by a series of identities. We can understand how that relation fits into the broader long- but finite-wavelength behavior of the correlators $\langle j_x(t)j_0(0) \rangle$ and $\langle \varepsilon_x(t)\varepsilon_0(0) \rangle$ by considering the pole structure of the Liouvillian of a large but finite system.⁷ Consider Fourier transforms of the energy and current operators

$$\begin{aligned} \varepsilon_k &\propto \sum_x e^{-ikx} \varepsilon_x \\ j_k &\propto \sum_x e^{-ikx} j_x. \end{aligned} \quad (\text{F1})$$

⁷ We take the system finite for convenience: so operators have discrete spectra. We also take the system to have periodic boundary conditions.

The Liouvillian \mathcal{L} is the linear operator generating a system's Heisenberg dynamics; it has a matrix element between general operators A, B

$$\langle A|\mathcal{L}|B\rangle = i\text{Tr}\left(A[H, B]\right), \quad (\text{F2})$$

where H is the system's Hamiltonian. A correlation function $\langle j_k(t)j_k(0)\rangle$, then, is

$$C^{jj}(k, t) = \text{Tr}[j_k(t)j_k(0)] = \langle j_k|e^{-i\mathcal{L}t}|j_k\rangle. \quad (\text{F3})$$

Since the dynamics is unitary, the Liouvillian \mathcal{L} is Hermitian. For any finite-sized system, the dynamics are thus described by a complete set of eigenvectors with real eigenvalues; this dynamics, however, includes recurrences in $C^{AB}(t)$ on timescales exponentially long in system size that do not occur in the thermodynamic limit.

For chaotic systems in the thermodynamic limit, correlations such as $\langle j_k(t)j_k(0)\rangle$ decay. [15, 17, 20] argue (with varying degrees of explicitness) that this should be understood in terms of a non-Hermitian effective Liouvillian \mathcal{L}_{eff} that matches the exact, Hermitian Liouvillian \mathcal{L} for local operators. DAOE [15] and the OST dynamics of [20] are two examples of such a non-Hermitian effective Liouvillian; we give details of the OST dynamics in Sec. III C. Here we assume \mathcal{L}_{eff} is diagonalizable. \mathcal{L}_{eff} again gives a correlation function $\langle A|e^{-i\mathcal{L}_{\text{eff}}t}|B\rangle$, but now \mathcal{L}_{eff} 's eigenvalues can have an imaginary part, leading to the observed decay. In the long-time limit only the slowest eigenvalues—those with smallest imaginary part—remain.

The diffusive phenomenology of the previous section appears in these slowest eigenvalues due to the constraints placed on the Liouvillian by translation invariance and the discrete continuity equation (3). Because the system is translation-invariant, the Liouvillian is block-diagonal in k space; call the blocks \mathcal{L}_k . The continuity equation (3) implies that in the small- k limit

$$\mathcal{L}_k|\varepsilon_k\rangle = k|j_k\rangle. \quad (\text{F4})$$

In terms of orthonormal vectors $|\hat{j}_k\rangle = \|j_k\|^{-1}|j_k\rangle$ and $|\hat{\varepsilon}_k\rangle = \|\varepsilon_k\|^{-1}|\varepsilon_k\rangle$, where $\|\cdot\|$ is the Frobenius norm, the

effective Liouvillian is

$$\mathcal{L}_k = a_k k |\hat{j}_k\rangle\langle\hat{\varepsilon}_k| + \text{h.c.} + M_k \quad (\text{F5})$$

where M_k acts on the space orthogonal to $|\varepsilon_k\rangle$, and $a_k = \|j_k\|/\|\varepsilon_k\|$ is a model-dependent constant. In this notation the Laplace-space memory matrix $M_{\varepsilon\varepsilon}(z)$ of 9 and 47 is

$$\begin{aligned} M_{\varepsilon\varepsilon}(z) &= i \langle j_k|(z + iM_k)^{-1}|j_k\rangle \\ &= ik^2 \int_0^\infty dt e^{-zt} \langle j_k|e^{-iM_k t}|j_k\rangle. \end{aligned} \quad (\text{F6})$$

That is, the memory matrix of 9, 42, 43, and 47 is the Laplace transform of the correlation function generated by our M_k , which captures the dynamics of j_k apart from the energy density.

For $k = 0$ the charge completely decouples from the rest of the dynamics, as expected from conservation; at small but nonzero k the coupling can be treated perturbatively. Expand $\mathcal{L}_{\text{eff},k}$ to leading order in k

$$\mathcal{L}_{\text{eff},k} = \mathcal{L}_{\text{eff},0} + kM'_0 + \left(a_0 k |\hat{j}_0\rangle\langle\hat{\varepsilon}_0| + \text{h.c.}\right) + O(k^2) \quad (\text{F7})$$

and call the perturbation $V = M'_0 + (ia_0 |\hat{j}_0\rangle\langle\hat{\varepsilon}_0| + \text{h.c.})$. Using second-order perturbation theory, we calculate the eigenvalue corresponding to the charge ε_k :

$$\lambda_\varepsilon(k) = a_0^2 k^2 \langle\hat{j}_0|\mathcal{L}_{\text{eff},0}^{-1}|\hat{j}_0\rangle. \quad (\text{F8})$$

This is the diffusive pole $z = Dk^2$. We can calculate its coefficient by integrating the total current autocorrelation function:

$$D = \frac{1}{\nu L} \int_0^\infty dt \langle J(t)J(0)\rangle \quad (\text{F9})$$

noting that $a_0^2 = \|J\|^2/\nu L$ from (9). This expression matches (12b) exactly.